Multivariate functionalization of UiO-66 for photocatalytic water remediation

Ainara Valverde[1,2], David Payno[1], Luis Lezama[3], José M. Laza[2], Stefan Wuttke[1,4,], and Roberto Fernández de Luis[1,*]*

Ms. A. Valverde, Mr. D. Payno, Prof. Dr. S. Wuttke, Dr. R. Fernández de Luis
[1]BCMaterials (Basque Centre for Materials, Applications & Nanostructures), Bld. Martina Casiano, 3rd. Floor UPV/EHU Science Park Barrio Sarriena s/n 48940 Leioa, Spain

Ms. A. Valverde, Dr. J. M. Laza
[2]Macromolecular Chemistry Group (LABQUIMAC), Department of Physical Chemistry Faculty of Science and Technology, University of the Basque Country (UPV/EHU), Barrio Sarriena s/n 48940 Leioa, Spain, 48013 Bilbao, Spain

Prof. Dr. L. Lezama
[3]Dept. of Inorganic Chemistry, Science and Technology Faculty, University of the Basque Country (UPV/EHU), Barrio Sarriena s/n, Leioa, Bizkaia 48940

Prof. Dr. S. Wuttke
[4]IKERBASQUE, Basque Foundation for Science, 48013 Bilbao, Spain
E-mail: roberto.fernandez@bcmaterials.net, stefan.wuttke@bcmaterials.net

Keywords: Multivariare metal-organic frameworks, photocatalysis, water remediation, hexavalent chromium

The fast-increasing interest in multivariate metal-organic frameworks (MTV-MOFs) has burgeoned due to the possibility to create synergetic functions and achieve performance significantly better than their simple sum. In this work, we explore the opportunities and the effects of multivariate functionalization of UiO-66 on diverse properties important for photocatalytic water remediation: hydrolytic stability, band gap energy, photoconduction, Cr^{VI} and Cr^{III} adsorption capacity and kinetics, and Cr^{VI} to Cr^{III} photoreduction efficiency. By developing (Zr)UiO66-NH_2-$(OH)_2$-NO_2 multivariate material based on the combination of 2-aminoterephthalate, 2,5-dihydroxyterephthalate and 2-nitroterephthalate organic linkers in

the same framework, we developed a dual sorbent/photo-catalyst for water remediation with excellent properties: (1) enhanced adsorption efficiency of Cr^{VI} and Cr^{III} ions; (2) improved photocatalytic conversion of Cr^{VI} to Cr^{III}; and (3) with suitable chemical stability under acidic conditions for the catalytic application. This work represents a milestone for an emerging class of reticular materials that can synergistically use the properties of individual functionalities to solve complex problems beyond just the water remediation application discussed in this paper.

1. Introduction

The hectic pace of technological development achieved during the XX and XXI centuries is directly related to water pollution.[1,2] Among the many organic and inorganic chemicals introduced into the water basins by anthropogenic activities, heavy metals are of particular concern.[3–5] Heavy metals, which are defined as any relatively dense metal or metalloid that persists in the long-term in an ecosystem and its organisms, include not only cationic forms of cadmium[6], mercury[7,8] and lead, but also anionic chromate oxyanions formed from hexavalent chromium (Cr^{VI}).[3,9,10]

Hexavalent chromium is particularly dangerous due to its carcinogenicity, teratogenicity, and acute toxicity[11–13], but in parallel, it plays a pivotal role in metal plating, metallurgy, and the tanning and textile industries[14], causing substantial industrial water pollution. Cr^{VI} is typically found in water media in the form of chromate oxyanions (such as $(H_xCrO_4)^{2-x}$ or $Cr_2O_7^{2-}$), which exhibit a net negative charge, high solubility and mobility, and hence, a long term persistence in the environment.[13,15] In fact, the technical limitations of current water remediation technologies to capture traces of chromate anions from water media arises from these properties.[16]

The photocatalytic reduction of hazardous Cr^{VI} to the less toxic and mobile Cr^{III} [17–20] has stood out as a particularly promising remediation strategy due to its effectiveness, low-cost and absence of addition and/or generation of secondary hazardous chemicals during the process.[13,21,22] However, one of the limiting issues of the photoreduction of Cr^{VI} is the poor efficiency to capture the Cr^{III} generated during photocataysts. This is specially relevant for the majority of the industrial acid eluents produced by the metallurgy and metal-plating industries, where the acidity of the media favours the Cr^{III} solubility.[23] To tackle this drawback, the development of a dual-action photo-catalyst that can both efficiently reduce Cr^{VI} to Cr^{III} and subsequently immobilize trivalent chromium is required.[24–27]

Metal-Organic Frameworks (MOFs) are promising candidates to meet these demand as they have a porous structure able to immobilize chromium and some of them show promising

photocatalytic properties.[28–33] Initial research on MOF applications was limited due to the low chemical stability of MOF structures. However, this landscape drastically changed with the discovery of hydrolytically stable and chemically robust Zirconium(IV) UiO-66 structure, which triggered the application of MOFs for water remediation purposes.[12,28–30,34–37] In addition, Zr-UiO-66 structure is built up from $Zr_6O_4(OH)_4(COOH)_{12}$ hexa-nuclear clusters that possess adsorption sites for oxoanionic species (including chromates).[15,38] The second advantageous feature of Zr-UiO-66 is that it functions as a semiconductor photocatalyst able to absorb UV-Vis light[14,39], which afterwards activates the metal sites by electron/hole transfer, and finally generates radical oxygen species that photo-reduce Cr^{VI} to Cr^{III} with incredible efficiency (Scheme 1a).

Nowadays, there are many studies that have enhanced either Cr^{VI} adsorption or photocatalytic performance of pre- or post-synthetically modified Zr-UiO-66 frameworks.[39,40] For example, amino and dihydroxyl functionalization endow UiO-66 with chemical (i.e. $-(OH)_2$) and photocatalytic (i.e $-NH_2$) capacity to reduce Cr^{VI} to Cr^{III}[14,21], as well as with the chemical affinity to adsorb both Cr^{VI} (i.e. $-NH_2$) and Cr^{III} (i.e. $-(OH)_2$). However, as concluded from X-ray diffraction data, both UiO-66-NH_2, UiO-66-$(OH)_2$ lack the chemical robustness to work under highly acidic or caustic conditions that only the nitro functionalized UiO-66-NO_2 can tolerate (Scheme 1b).[41] Nevertheless, the loss of the long-range ordering of the MOF material (*determined by X-ray diffraction*) is not the only parameter that accounts for their overall chemical stability. The partial release of the organic linkers or metals of the framework when the MOF materials are immersed under slightly acidic or basic solutions, is as well a key parameter to assess their chemical strength. For instance, the partial leaching of the MOF constituents does not preclude the structural collapse of the material, which under most of the conditions maintains its X-ray diffraction fingerprint, leading to conclusions that are not entirely precise regarding its chemical and hydrolytic stability.

Recently, multivariate functionalization strategy has emerged, offering an opportunity to tailor and balance all the targeted characteristics to achieve a fast and efficient Cr^{VI} to Cr^{III} photoreduction via the synergistic combination of different functional groups (Scheme 1). Multivariate MOFs (MTV-MOFs) possess more than two functionalities randomly distributed within the framework that work together in a cooperative fashion, outperforming—as an ensemble—their homogenous and periodic counterparts.[42–52] In other words, the synergistic performance of a MTV-MOF (outperforming the homogenous and periodic counterparts) is the key criteria. However, introducing compositional variance in crystalline compounds brings new challenges, such as the exploration of the vast chemical space of functionalities variance and

distribution that results in a cooperative performance and distinguishing multivariance from statistical disorder.[45][53] In practice, reticular chemistry introduces variance synthetically or post-synthetically towards optimizing for a particular function.[35,54,55] This requires the identification of a structure, its constituents, and possible compositional and structural variabilities (such as metals, organic linkers, absence of linkers, etc. that are compatible with the structure's integrity). Ideally, variants that could aid in performing a specific task are identified.[33] Furthoremore, up to date, the impact of the chemical variance on the thermal or chemical/hydrolytic stability and photocatalytic properties of MTV-MOFs are fairly unexplored.

In this paper, we employed the multivariate functionalization strategy to tune multiple chemical characteristics of UiO-66 structure, such as the light harvesting, adsorption capacity over Cr^{VI} and Cr^{III} species, photoconduction efficiency, and Cr^{VI} to Cr^{III} chemical reduction and photoreduction properties. In parallel, we explored how the compositional variance in MTV-MOFs affects their hydrolytic stability in comparison to the one of their parent single-functionalized frameworks (Scheme 1). From the overall performance to photoreduce and capture chromium ions, the balanced multivariate functionalization of the UiO-66-NH_2/-$(OH)_2$/-NO_2 framework has resulted in a dual sorbent/photo-catalyst with: (1) efficient chemical/photo reduction of Cr^{VI} to Cr^{III} and (2) retention through adsorption of the resulting Cr^{III} ions (Scheme 1c). When considering the hydrolytic stability of the MTV-frameworks, although the leaching of the organic linkers is attenuated in comparison to the single functionalized UiO-66 frameworks (specially in comparison to -NO_2 and -$(OH)_2$ variants), there is still a significant selective release of nitro and dihydroxy terepththalate linkers under acidic or basic conditions, even when the structural stability of the compounds is maintained, as confirmed by X-ray diffraction. Overall, this work shows the high potentials, but also the limitations in terms of thermal and chemical stability, of multivariate functionalization strategy to create synergetic properties and functions for targeted applications. Although the study is focused on the MTV-MOF application for water remediation purposes, it could be expanded to other case studies far from water remediation such as gas or vapour adsorption in humid conditions, chromatographic separation or catalysis performed in liquid media.

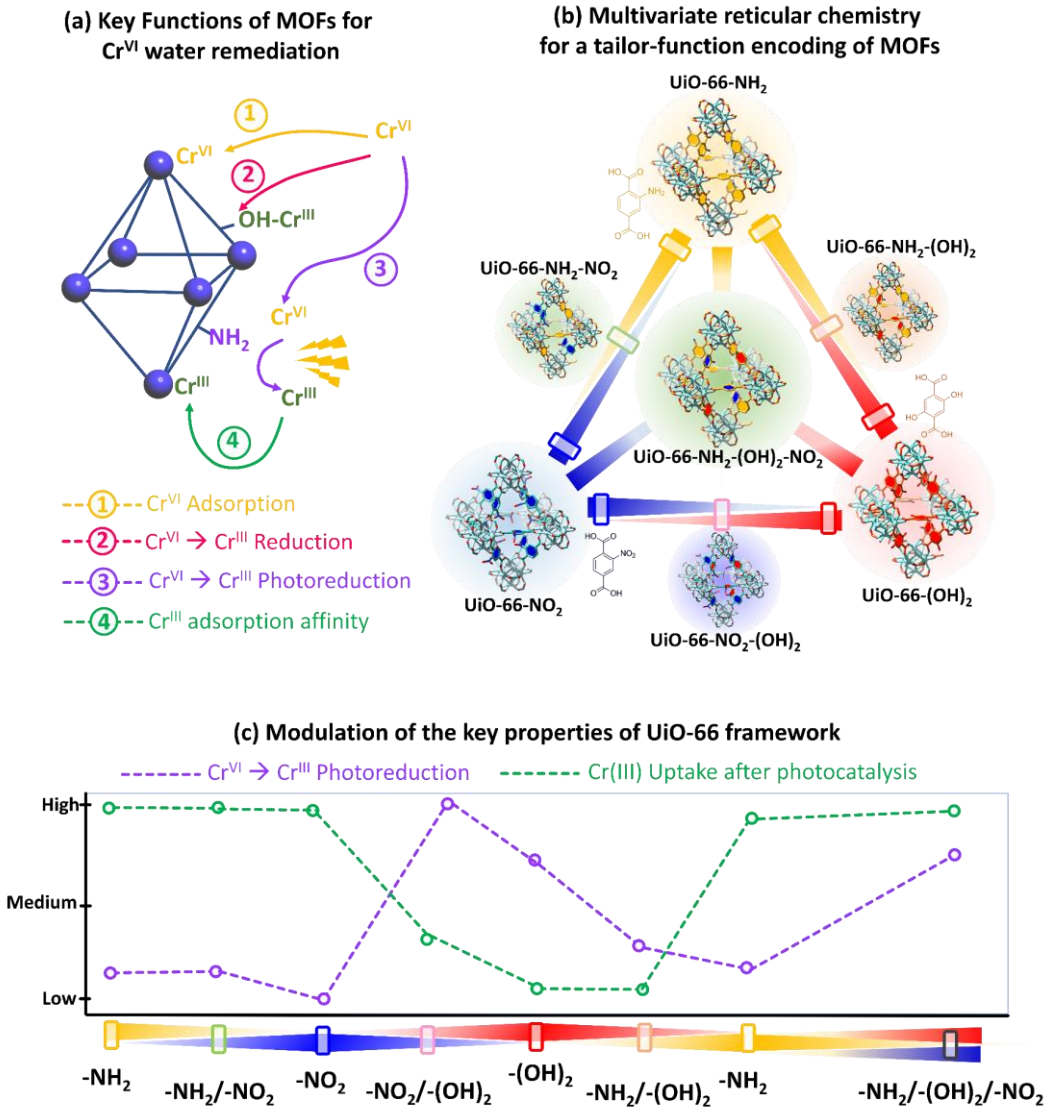

Scheme 1. (a) Key functions needed in MOF materials for the Cr^{VI} to Cr^{III} capture and transformation. (b) Multivariate encoding strategy of the UiO-66 framework developed in this work. (c) Modulation of the key properties of the UiO-66 variants depending on their single and multivariate functionalities.

2. Results and Discussion

2.1. Synthesis and general characterization of single and multivariate MOFs.

UiO-66-R with single functionalities (R= $-NO_2$, $-NH_2$, and $-(OH)_2$) were obtained through a solvothermal reaction following the protocol described by Audu *et al.*[56] Multivariate UiO-66 frameworks were synthesized using an equimolar mixture of the organic linkers. The same concentration of zirconium chloride and volume of N,N´-dimethylformamide used in the synthesis of single functional UiO-66 frameworks were maintained to obtain bi and tri-functional MOFs. After solvothermal treatment (80 °C, 24 h), the samples were recovered by

centrifugation, thoroughly washed with N,N-dimethylformamide, and afterwards, the solvent was exchanged with methanol once daily over three days. After activating the samples at 80 ºC overnight, the quality, particle size, porosity, thermal stability and optical properties of the single and multivariate MOFs were fully characterized by X-ray diffraction, infrared spectroscopy, scanning electron microscopy, ^{1}H-NMR, thermogravimetric analysis, surface area measurements and UV-Vis spectroscopy.

The comparison of the experimental and simulated X-ray diffraction patterns confirms that the single and multivariate compounds crystallize as the "fcu" cubic form of the well-known UiO-66 MOF (Figure 1a). The absence of impurities related to other crystalline phases was verified by full profile pattern matching analysis of the X-ray diffraction data, taking into account the cell parameters and space group of the UiO-66 parent structure (Figure S1-S7). Our data showed almost identical cell parameters, with only slight variations in the values of the full width at half maximum of the patterns. As confirmed by scanning electron microscopy, this divergence can be explained by the variation of the particle size of the samples (Figure S8).

FTIR spectra show the characteristic fingerprint bands of the UiO-66 framework, as well as those of the -NH_2, -NO_2 and -$(OH)_2$ functionalities within the single and multivariate materials (Figure 1b). There is no significant shift in the vibrational frequencies from the single-functionalized to the multivariate frameworks. Some of the most characteristic vibrational modes common to all the UiO-66-R (R= -NH_2, -$(OH)_2$, - NO_2, -NH_2/-$(OH)_2$, -NH_2/-NO_2, -$(OH)_2$/-NO_2 and -NH_2/-(OH_2)/-NO_2) frameworks studied in this work are the longitudinal and transverse vibration of the Zr-O bonds (at 745 and 660 cm^{-1})[57] and/or to the asymmetric and symmetric stretching vibrations of the carboxylate groups (1581 and 1389 cm^{-1}).[36]

Once the presence of the amino, nitro, and hydroxyl functional groups within the single and multivariate materials was confirmed by IR spectroscopy, their molar ratio was calculated using ^{1}H-NMR analysis of the digested samples (Figure 1c and Table 1). For the MTV-MOFs, the linkers´ molar ratio (as obtained from integration of the ^{1}H-NMR data) aligns with the expected value, although there was a slight preference for the incorporation of nitro-linkers over the amino and dihydroxyl, and of the amino-linkers over the dihydroxyl.

The micropore surface areas obtained by analyzing nitrogen adsorption isotherms at low-pressure are lower in comparison to the values reported in literature. Instead, the surface area of our samples seems to be linked to the external area of the nanoparticles in the mesoporous regime (Figure S16).[58,59] The similarity to isotherm types I/II or I/IV is consistent with a microporous solid formed by nanoscopic particles that have meso/macro-porous-sized gaps

between them. For instance, the external surface area of the particles can be qualitatively correlated with the particle size observed by scanning electron microscopy (Figure S8).

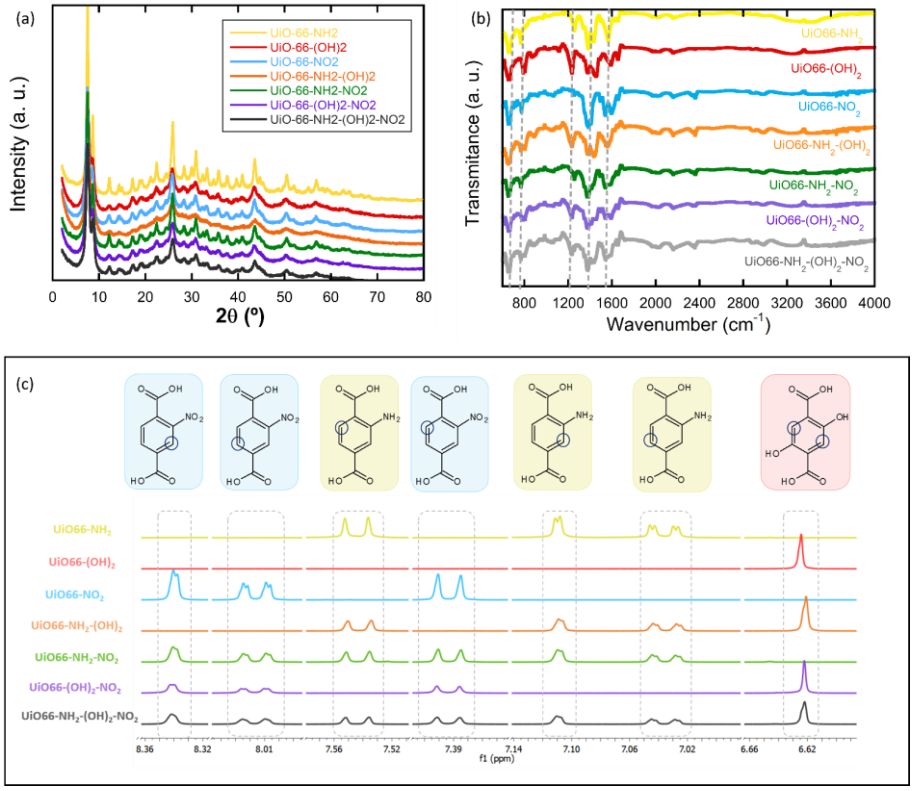

Figure 1. (a) XRD pattern, (b) IR and (c) ^{1}H-NMR spectra for UiO-66-R materials.

Table 1. Molar ratio of BDC-NH_2, BDC-$(OH)_2$ and BDC-NO_2 linkers in single and multivariate UiO-66 frameworks.

	BDC-NH_2 Synthesis/Material*	BDC-$(OH)_2$ Synthesis/Material*	BDC-NO_2 Synthesis/Material*
UiO-66-NH_2	100 % / 100 %	0 % / 0 %	0 % / 0 %
UiO-66-$(OH)_2$	0 % / 0 %	100 %/ 100 %	0 % / 0 %
UiO-66-NO_2	0 % / 0 %	0 % / 0 %	100 % / 100 %
UiO-66-NH_2-$(OH)_2$	50 % / 56 %	50 % / 44 %	0 % / 0 %
UiO-66-NH_2-NO_2	50 % / 46 %	0 % / 0 %	50 % / 54 %
UiO-66-$(OH)_2$-NO_2	0%	50 % /41 %	50 % / 59%
UiO-66-NH_2-$(OH)_2$-NO_2	33 % / 34 %	33 % /26 %	33 % / 40 %
• Molar percentage of the linkers in the reaction media and incorporated to the UiO-66-R material.			

As explained in the following sections, the thermal and chemical stability, light harvesting capacity and photoconduction efficiency of the single and multivariate UiO-66 frameworks are all affected by the type and amount of the functional groups. Overall, the chemical variance of MTV materials improve their efficiency to capture and photoreduce chromium species, but affects as well their hydrolytic stability, especially at acidic and basic conditions.

2.2. Multivariate modulation of the thermal and chemical stability

The thermal stability of the UiO-66 frameworks was evaluated through thermogravimetric analyses. The thermogravimetric profiles of MTV-UiO-66 samples are close to the average sum of the TGA signal of single-functionalized materials. Therefore, the thermal stability of MTV-UiO-66 materials is governed by the functionality with the lower thermal resistance (Figure S9-S15). For the single-functionalized materials, the calcination process of the organic linker, usually associated with the thermal collapse of the framework, begins at 360 °C, 320 °C, and 295 °C for UiO-66-NH_2, UiO-66-$(OH)_2$, and UiO-66-NO_2, respectively (Figure S9-S11). By contrast, in MTV materials, the thermal collapse begins at almost the same temperature as the collapse of the corresponding singly functional framework with the lower thermal stability (i.e. UiO-66-NH_2-NO_2 → 320 °C, UiO-66-NH_2-$(OH)_2$ → 300 °C, UiO-66-$(OH)_2$-NO_2 → 300 °C and UiO-66-$(OH)_2$-NO_2-NH_2 → 310 °C) (Figure S12-S15). These results confirm that the thermal resistance of MTV-MOFs is defined by one - the weakest link in the chain - of the functionalities. The quantitative analysis of the thermogravimetric curves (specifically the weight loss associated with the calcination of the organic linker) display that all smaples have approximately 0.5 linker defects per formula unit. This is an important structural feature, since defect chemistry promotes the adsorption of chromate anions. Therefore, having a similar density of linker-defects within the studied material assures that the differences observed in their properties (e.g. adsorption capacity and kinetics, photocatalysis, photoconduction…) arises from the single or multivariate functionalities installed in the framework.

In order to study the chemical stability of the single and multivariate functionalized UiO-66 materials, 30 mg of the MOF were immersed in 15 mL of aqueous solutions with different acidities (pH= 4, 7, 9 and 12) for 24 hours. After that, the solid was collected by centrifugation and measured by XRD, and the supernatant was kept for its study by UV-Vis spectroscopy. The X-ray diffraction patterns of the single and multivariate UiO-66 materials immersed at slightly acidic to basic aqueous media (pH 4 to 9) do not show significant changes in comparison to the initial ones (Figure S19-S25). This is not the case for the XRD data of the samples exposed to basic solutions of pH=12, which point that the long-range ordering of the frameworks is lost during the process. This results match with expected ones, as the structural stability of the UiO-66 family in aqueous media has been corroborated in many works by X-ray diffraction.[41,60–64] However, this data can not be used alone to positively claim that no fraction of the sample has been partially destabilized/dissolved giving rise to a leaching of the organic linkers and zirconium ions to the aqueous media.[60,65]

Further stability tests from pH 4 to 9 were carried out by using UV-Vis spectroscopy, in order to monitorize the linker amount in the solution, as any leaching of the organic linkers to the solutions above a concentration of 1 $mg \cdot L^{-1}$ would be detectable via UV-Vis, as shown in the Figure 2 and Figures S26-S29. Even though the absorbance values of the UV-Vis spectra give us only a comparative estimation of the organic linkers concentration leached from the MOF into the aqueous media (Figure S30), we have tried to semiquantify this information. To this end, a calibration curve was built for the amino, dihydroxy and nitrotherephtalic aqueous solutions at 250 nm for all samples and at 350 nm in the specific case of amino and dihydroxy linkers (Figure S31 – S33). Therefore, on the basis of the calibration curves, we can estimate in a semiquantitiave manner the concentration of the linkers leached from the single functionalized MOFs. For the single functionalized UiO-66-NH_2, UiO-66-$(OH)_2$ and UiO-66-NO_2 samples, this can be easily calculated with this calibration curve. However, for the MTV MOFs a slightly longer procedure is used, which is detailed in the SI section 3.2.

The percentage of the organic linkers leached from the MOF was calculated as detailed in the equation 1 and in a more detailed way in SI-section 3.2):

% of linkers released *= 100 x (concentration of the linker determined by UV-Vis ($mg \cdot L^{-1}$))/ total concentration of the linker if all the MOF sample is dissolved ($mg \cdot L^{-1}$)* *Eq. 1.*

It is important to mention that our approach is a qualitative one to estimate the chemical robustness of UiO-66 frameworks, and in general of MOF materials, which organic linkers or metals give a UV-Vis signal when dissolved in water (or other organic solvents). This makes the methodology easily accessible for the research community working on MOF materials, although less accurate than the quantification of the linkers concentration through liquid chromatography.

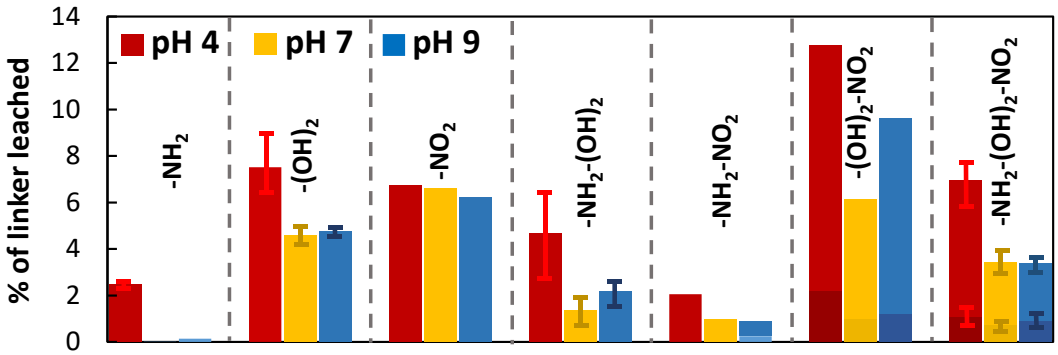

Figure 2. Percentage of the organic linkers dissolved when after immersing 30 mg of MOFs in 15 mL of aqueous solutions (pH= 4, 7 and 9) during 24 h.

UV-Vis spectroscopy confirms that even if the crystallinity of the samples is maintained, there is a partial leaching of the linkers into solution for all samples between pH 4 and 9, but the value of this figure is highly dependent on the functional groups presence in the frameworks. UiO-66-NH_2 shows the smaller release of amino-terephthalate linkers into the solution (nearly negligible at pH 7 and 9, and close to 2% at acidic conditions (i. e. pH 4)) in comparison to the ones observed for UiO-66-NO_2 and UiO-66-$(OH)_2$ (from 5 to 7.5 %). In contrast, UiO-66-$(OH)_2$ and UiO-66-NO_2 release significant amounts of their linker to the solution, especially at acidic conditions (> 6 %). For MTV-MOFs, the hydrolytic stability is approximately an average of the one reported for their single functionalized materials. The samples with amino functionalities are the ones that show the lower degree of linker release. For instance, UiO-66-NH_2-NO_2 exhibits a selective loss of nitro-terephthalate linkers (< 2%) and a negligible release of amino-terephtalate structs at acidic and neutral conditions (as concluded by the absence of the UV-Vis absorption band located at 350 nm). UiO-66-NH_2-$(OH)_2$ shows intermediate values between the ones observed for UiO-66-NH_2 and UiO-66-$NH_2(OH)_2$. The release of organic linkers in UiO-66-NO_2-$(OH)_2$ and UiO-66-NH_2-NO_2-$(OH)_2$ is accentuated in comparison to their single functionalized counterparts. For instance, in these two case studies we were able to roughly differentiate the BDC-NO_2 and BDC-NH_2/$(OH)_2$ leaching to the media, but the final values need to be considered carefully. Nevertheless, the overall percentage of organic linkers released to the aqueous media excess in UiO-66-NO_2-$(OH)_2$ and UiO-66-NH_2-NO_2-$(OH)_2$ the sum of the values obtained for the single-functionalizable materials. When comparing the results obtained in this study with the tendencies reported in previous works, we found that our findings gives a complementary information. For instance, the structural stability of UiO-66-NH_2[62] and UiO-66-NO_2[66] when exposed to acidic and basic conditions have been previously corroborated, but this does not preclude that a partial release or dissolution of the MOF materials occurs during the process, as confirmed in our study. In parallel, as far as we know, this is the first time the corresponding data has been reported for the UiO-66-$(OH)_2$ homologue. Overall, it has been confirmed that the incorporation of amino functionalities to MTV-UiO-66 add chemical robustness to the frameworks by preventing amorphization but does not fully block the partial and selective release of nitro and dihydroxyl organic linker to the media.

2.3. Multivariate modulation of the light harvesting and photoconduction of UiO-66 frameworks

The light-harvesting capacity of the materials was studied by UV-Vis spectroscopy of solid samples (Figure S17). The absorbance data was transformed into $(\alpha hv)^2$ *vs.* energy plots to calculate the band gaps of the single and multivariate MOFs (Figure 3a-d). Three absorption bands were observed in the UV-Vis spectra: *i*) the first two were ultraviolet wavelengths, (likely from the charge transfer between the organic linkers and zirconium hexa-nuclear clusters) and *ii*) the third band was located in the visible range, and therefore can be assigned to the color of the amino and dihydroxyterephthalic linkers. As expected, the white colored UiO-66-NO_2 shows the highest band gap value, 3.26 eV, demonstrating its capacity to harvest light exclusively in the ultraviolet energy range. UiO-66-NH_2 (2.84 eV) and UiO-66-$(OH)_2$ (2.75 eV) have smaller band gaps, suggesting that they can harvest light in the range of visible blue light. In the most cases, the MTV-MOFs exhibit band gaps slightly lower than the average value calculated from the band gaps of single-functional MOFs. UiO-66-NH_2-$(OH)_2$ is an exception to the general trend; it outperforms its calculated band gap of by 0.15 eV, and also the band gaps of the UiO-66-NH_2 and UiO-66-$(OH)_2$ materials. Therefore, MTV chemistry allows us to tune not only the semi conduction band by selecting the proper functional groups, but to also manipulate synergistic effects to improve the light harvesting capacity of the parent, singly functional MOFs (Figure 3f). Mott-Schottky plots were performed to investigate the flat band potential as well as Fermi energy level of the materials. As shown in Figure S18, the positive slopes of the Mott-Schottky plots exhibit the typical n-type semiconduction. The flat band potentials are around -0.5 V *vs.* Ag/AgCl, which is in good agreement with previous researches.[67,68] In general, the flat band potential of n-type semiconductor (intercept value at the x-axis) can be used to estimate the conduction band (CB) of the semiconductor.[69] The CB potential of the UiO-66-R single and MTV materials (around -0.5 V *vs.* Ag/AgCl) is more negative compared to the $O_2/O_2^{-\cdot}$ (-0.13 V *vs.* Ag/AgCl), and thus, they can reduce the adsorbed O_2 to form $O_2^{-\cdot}$.[70], and it is also more negative than the Cr^{VI} to Cr^{III} reduction potential (+1.15 V *vs.* Ag/AgCl), allowing the material to perform this reduction process.[68]

The photocurrent response of the materials was also measured under intermittent light irradiation (Figure 3e). Among the single encoded UiO-66, UiO-66-$(OH)_2$ shows the best photoconduction as a consequence of encoding an electron-donor group into the structure that provides the linkers of free electrons, and thus, increases its conductivity. For the MTV-MOFs, it is noticeable than when BDC-$(OH)_2$ is combined with BDC-NO_2 a huge increase in the photoconductivity is observed. This can be due to the combination of electron donor and electron acceptor groups in the same structure, which increases the electron flux through the framework. Between the two materials with best photochemical response, a shape difference

can be seen. UiO-66-$(OH)_2$-NO_2 shows a wave-like profile, characteristic of materials with slower photo-response, as it needs more time to rise its maximum photoconduction when it is illuminated. On the other hand, UiO-66-NH_2-$(OH)_2$-NO_2 exhibits a square-like shape, characteristic of a very quick photochemical response, achieving its maximum photoconduction rate in less than a second.

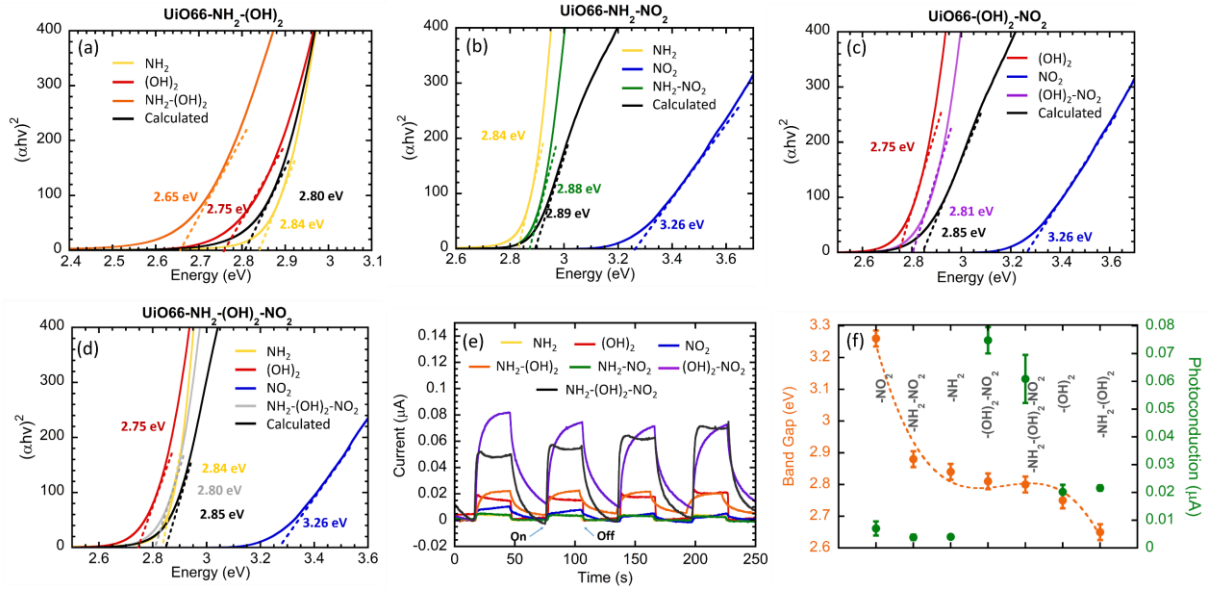

Figure 3. (a-d) Tauc plots and calculated band gaps for single functionalized and multivariate MOF. Black lines account for the calculated Tauc plot of the MTV-MOF from the averaged sum of the single functionalized UiO-66 frameworks. (e) Photocurrent response under intermittent light irradiation for single and multivariate encoded UiO-66 frameworks. (f) Band gap and photoconduction values for single and multivariate encoded UiO-66 frameworks.

2.4. Modulation of the dual Cr^{VI}/Cr^{III} adsorption

The adsorption kinetics of single and multivariate UiO-66 materials over Cr^{VI} and Cr^{III} species were assessed with 15 ppm chromium solutions (Figure 4a-b). Note that a sorbent dosage of 0.5 $g \cdot L^{-1}$ was used in these experiments because this value is within the operative photo-catalyst dosage (0.25 – 1 $g \cdot L^{-1}$) that will be used later for the Cr^{VI} to Cr^{III} photoreduction experiments. The adsorption kinetics were performed under acidic conditions (pH = 4) which prevents the precipitation of Cr^{III} oxides/hydroxides during dark and illumination conditions. The experimental data and its fitting with a pseudo-second order kinetic model have been plotted in Figure 4a-b. The Cr^{VI} and Cr^{III} adsorption capacities and kinetic rates have been summarized in the Figure 4c-d.

As previously mentioned, Cr^{VI} is stabilized at acidic pH values as dichromate ($Cr_2O_7^{2-}$) and hydrogen-chromate ($HCrO_4^-$) anionic species. All of the UiO-66-R materials studied exhibit

interesting Cr^{VI} adsorption capacities because of the presence of uncoordinated positions derived from linker defects. At first sight, the amino decorated MOF is the one of the UiO-66 variants that exhibits the best adsorption capacity over Cr^{VI} (Qe = 15.5 mg·g^{-1}). This increased absorption capacity can be explained by the electrostatic interactions between the protonated NH^{3+} groups and the chromate anions, as reported previously by S. Rapti *et al.*[71] Hydroxyl, nitro and MTV materials show similar Cr^{VI} loading values at equilibrium, ranging from Qe = 6 to 8 mg·g^{-1} (Figure 4a). It is interesting to note that the kinetics of Cr^{VI} adsorption are strongly affected by the MTV chemistry, as shown by the *k* values obtained from the pseudo second order modelling (dashed lines in Figure 4a and b) used to fit the experimental data (Figure 4c). For instance, single and MTV UiO-66 frameworks encoded with hydroxyl functionalities exhibit slower kinetics, likely due to the steric and electrostatic repulsions arising from the hydroxyl groups and chromate oxyanions (Figure 4c). Overall, amino and/or nitro functionalized UiO-66 variants are the strongest candidates for the Cr^{VI} capture in terms of adsorption capacity and kinetics, respectively.

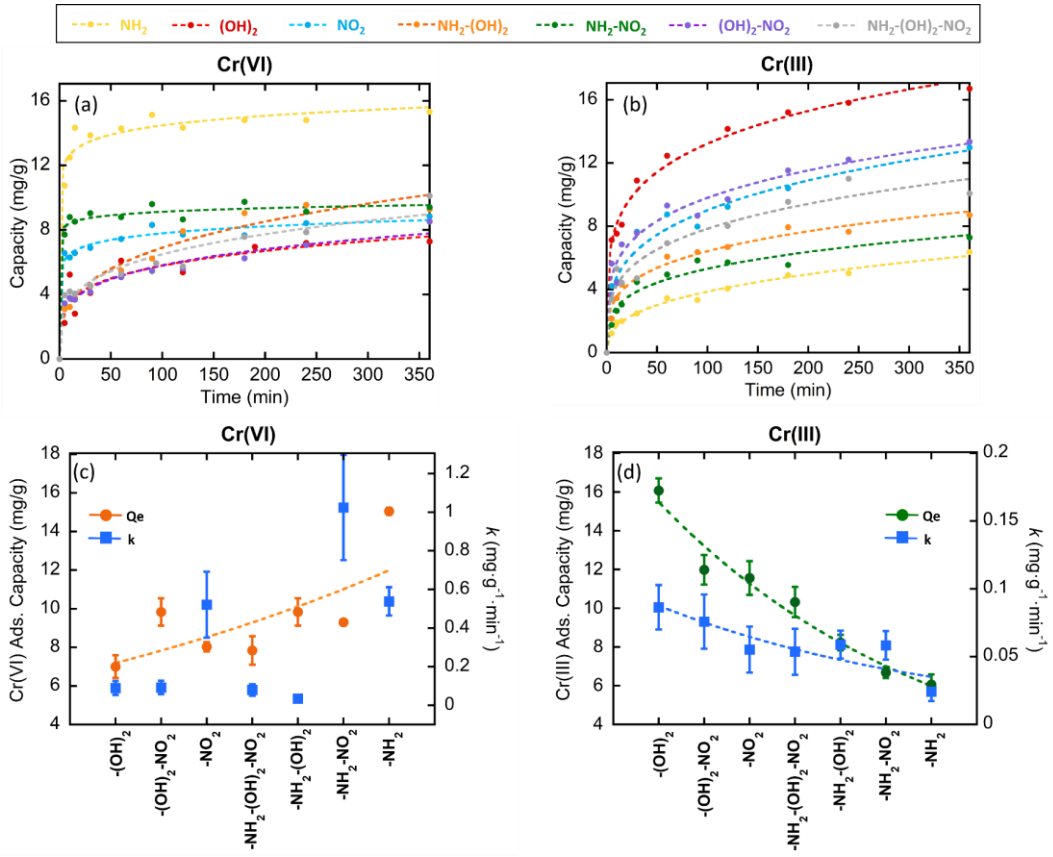

Figure 4. Adsorption kinetics over (a) Cr^{VI} (5 ppm) and (b) Cr^{III} (5 ppm) for UiO-66 type materials. Q_e and *k* values obtained by fitting the experimental data for (c) Cr^{VI} and (d) Cr^{III} adsorptions to a pseudo second order model. Dashed lines in (a) and (b) correspond to the fitting

curve obtained from the application of a pseudo-second kinetic model to the experimental data (circles).

The trend is almost perfectly reversed for Cr^{III} cations. In general terms, the profiles of the kinetics of Cr^{III} adsorption suggest slower uptakes in comparison to Cr^{VI} (Figure 4b). Dihydroxyl (Q_e = 16.5 mg·g^{-1}) and/or nitro (Q_e = 12.5 mg·g^{-1}) functionalized UiO-66 variants show the best performance to capture Cr^{III} in terms of adsorption capacity and kinetics, although *k* rates are at least two-fold smaller than in Cr^{VI} adsorption. Most importantly, MTV chemistry opens proves to be an excellent and unique tool for fine modulation of both the capacity and kinetics of the Cr^{III} capture (Figure 4d).

2.5. Dual photocatalytic and adsorptive capacity

Once the ability of MTV-UiO-66 family to adsorb Cr^{VI} and Cr^{III} was assessed, their capacity to photo-reduce Cr^{VI} to Cr^{III} under UV irradiation was studied (Figure 5a-d). First, an initial adsorption in darkness was performed with Cr^{VI} solutions of specific concentrations between 14 and 12 mg·g^{-1}. The initial point of the experiment was adapted to each material in order to obtain the most similar Cr^{VI} concentration after adsorption stage, and hence, as the starting point of the photocatalysis experiments. This point is relevant for later quantitative comparison of Cr^{VI} to Cr^{III} photocatalysis kinetics, since this parameter depends on the initial substrate concentration. Once equilibrium is reached after adsorption, the Cr^{VI} to Cr^{III} photoreduction is triggered by the illumination of the catalysts with a 365 nm UV-lamp. The experimental results of the multivariate compounds and of the UiO-66 compounds with single-functionalities are shown in Figure 5a-d. In experiments, the change in Cr^{VI} and Cr^{III} concentration was monitored during both the adsorption and photocatalysis steps. The rates of Cr^{VI} to Cr^{III} photo-reduction in the single and multivariate samples were obtained after the fitting of the experimental data to a first-order kinetic model (Figure S36-37). The photoconduction values and the photocatalysis rates have been summarized in Figure 5e and Figure S38. In addition, the Cr^{III} release has been correlated with the hydrolytic stability of the frameworks, and specially with the release of BDC-$(OH)_2$ linker to the media, with the Cr^{III} concentration detected after the photocatalysis experiments. In order to study the effect of the initial Cr^{VI} concentration in the photoreduction rate, additional experiments were done for UiO-66-NH_2-$(OH)_2$-NO_2 at 5 and 30 mg·L^{-1} (Figure 5f).

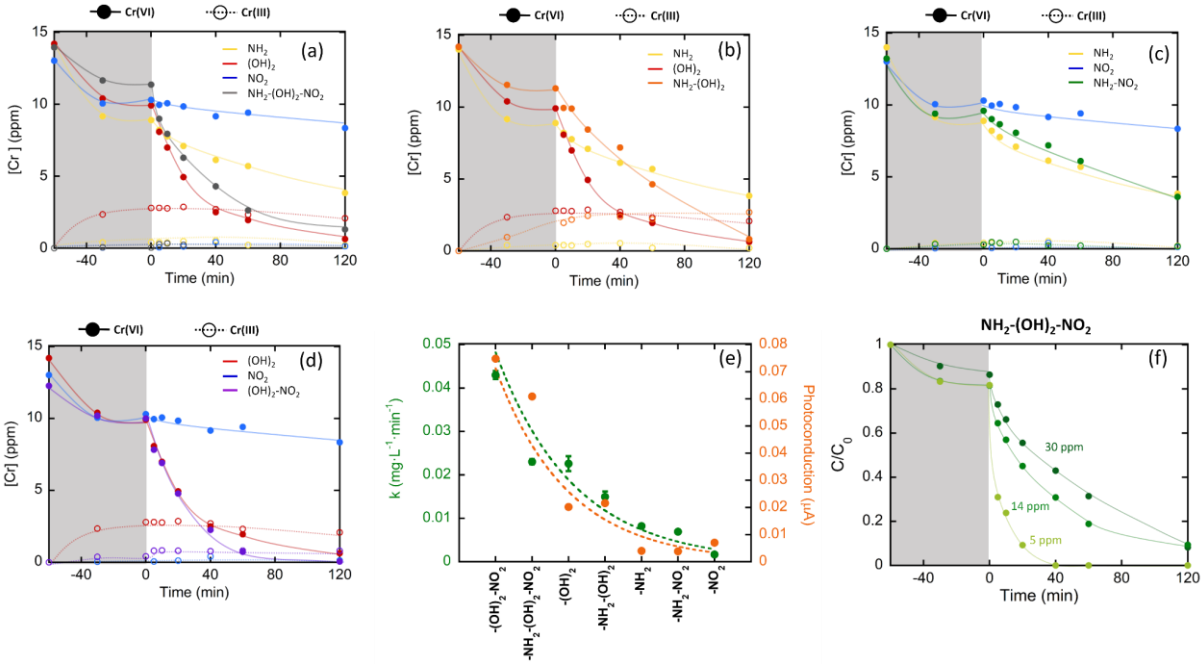

Figure 5. (a-d) Cr^{VI} to Cr^{III} photocatalytic reduction by single functionalized and multivariate UiO-66 materials. (e) Comparison between the Cr^{VI} to Cr^{III} photo-reduction rates and band gap values for the studied materials. (f) Cr^{VI} to Cr^{III} photocatalytic reduction for UiO-66-NH_2-$(OH)_2$-NO_2 material starting at different Cr^{VI} concentrations.

First, UiO-66-NO_2 (Figure 5a) shows negligible photoreduction activity when illuminated (~10 % of Cr^{VI} → Cr^{III}). By comparison, UiO-66-NH_2 (Figure 5a) shows that 50% of the Cr^{VI} was eliminated after 2 hours of UV-illumination. The experiments conducted with both UiO-66 variants show a negligible amount of Cr^{III} in the solution during the adsorption and photo-reduction stages. Therefore, the Cr^{III} species generated during photocatalysis are retained within the MOF, and not released into the media. Photocatalysis efficiency is even better for UiO-66-$(OH)_2$ (Figure 5a), which reduces almost the 99% of Cr^{VI} to Cr^{III} in 2 hours. Unfortunately, UiO-66-$(OH)_2$ shows an appreciable release of Cr^{III} during adsorption step even though this UiO-66 variant has the best Cr^{III} adsorption capacity (as demonstrated in kinetic experiments). The outstanding Cr^{III} adsorption and Cr^{VI} to Cr^{III} photo-reduction performance of the hydroxylated framework proves that it exhibits both photoreduction and chemical reduction functions. In return, the low hydrolytic stability of the framework gives rise to a release of di-hydroxylated terephthalic molecules (and therefore also the the Cr^{III} ions previously held at the hydroxyl sites) into the aqueous acidic media. However, it is clear that Cr^{III} concentration remains stable during photocatalysis, suggesting that an equilibrium between the MOF and the media is established once a certain concentration of dihydroxyterephthalate linkers is released. Multivariate UiO-66-NH_2-$(OH)_2$ shows a 99 % Cr^{VI} to Cr^{III} photoreduction efficiency, but with

slightly slower photo-reduction kinetics (Figure 5b) in comparison to UiO-66-$(OH)_2$. In parallel, a dual-stage Cr^{III} release has been observed during adsorption and photocatalysis. The Cr^{III} released in darkness (~ 1.2 $mg \cdot L^{-1}$) is between the negligible values obtained for UiO-66-NH_2 and the 2.5 $mg \cdot L^{-1}$ observed for UiO-66-$(OH)_2$. After UV-illumination, a second Cr^{III} release occurs, plateauing at a concentration of 2.5 $mg \cdot L^{-1}$, mirroring the observations of the UiO-66-$(OH)_2$ experiment. It is still unclear whether the Cr^{III} release is related to: (i) a destabilization of the MOF,or (ii) the limited capacity of the framework to retain the Cr^{III} ions generated during the photocatalysis. Given the good Cr^{III} adsorption capacity of UiO-66 variants containing hydroxyl functions, the first hypothesis seems to be the most plausible.

The Cr^{III} release during Cr^{VI} adsorption and photocatalysis is partially blocked when nitro-terephthalic linkers are included n the multivariate MOFs. As an illustrative example, UiO-66-NH_2-NO_2 is able to retain the Cr^{III} ions generated during photocatalysis while its photoreduction kinetics and efficiency are as good as UiO-66-NH_2, but still far inferior to UiO-66-$(OH)_2$ (Figure 5c). Conversely, dihydroxy- and nitro-terephthalate linkers act synergistically in the UiO-66-$(OH)_2$-NO_2 framework (Figure 5d), where we discovered that photoreduction activity becomes as good as UiO-66-$(OH)_2$, but Cr^{III} retention is improved by the stabilizing nitroterephthalate linkers. Even though Cr^{III} release is minimized when nitro and hydroxyl functions are encoded within the material, an appreciable 1.5 $mg \cdot L^{-1}$ Cr^{III} concentration is observed during the experiment. To address this, we encoded the nitro, amino and hydroxy functions in the same MTV-UiO-66 framework, which exhibits both excellent Cr^{VI} to Cr^{III} chemical reduction and photoreduction kinetics similar to UiO-66-$(OH)_2$, and negligible Cr^{III} release to the media as exhibited by UiO-66 variants containing nitro and/or amino functionalities.

When comparing the Cr^{III} release observed during the photocatalysis experiments to the chemical stability of the compounds, it is clear that these factors are closely correlated in the case of hydroxyl bearing linkers. For the nitro homologues, the correlation is not so evident. Despite the chemical stability studies show that there is a significant BDC-NO_2 release to the media, there is not an Cr^{III} concentration increase during photocatalysis. This evidence could be related with the lack of an important role of the nitro functions to adsorb Cr^{III} ions, so their release does not induce the loss of the Cr^{III} ions immobilized at the UiO-66 amino and hydroxyl functionalities. For instance, the higher the hydroxy and amino therepthalate linkers leached to the media, the more accentuated the Cr^{III} release during adsorption and photo-catalysis.

Multivariate chemistry of MOFs in the UiO-66 family gives rise to synergic effects in their photocatalytic performance. The photoconduction efficiency of the single and multivariate

materials is closely correlated with their efficiency in transforming Cr^{VI} to Cr^{III}. For instance, these materials containing hydroxyl groups exhibit faster kinetics to photo-reduce Cr^{VI} to Cr^{III}, although they exhibit significant Cr^{III} release during adsorption and photocatalysis stages. When balancing the chemical and photoreduction capacity with hydrolytic stability, tri-functional MTV UiO-66-$(OH)_2$-NH_2-NO_2 exhibits the best performance; in addition to superior photoreduction kinetic rates rivalling the hydroxyl variant. For instance, this trifunctional MTV-variant is able to retain the photo transformed Cr^{III} species with the same efficiency as the amino functionalized material (Figure 5a), even if significant leaching of nitro linkers has been observed.

In order to study how the initial Cr^{VI} concentration affects the photoreductive activity of UiO-66-NH_2-$(OH)_2$-NO_2, extra photocatalysis experiments were performed, starting at 30 ppm and 5 ppm (Figure 5f). The adsorption process in darkness remains similar, however, when the UV-lamp is turned-on, some differences can be observed. As it can be observed in Figure S38, the material show better kinetic rates at low Cr^{VI} concentrations (5 ppm > 15 ppms > 30 ppms), as more catalytic sites per Cr^{VI} ions are accessible for their photoreduction. Starting from a Cr^{VI} 5 ppm solution, 100% of the chromium can be eliminated in only 40 minutes. This photoreductive response fits with the usuall chromium concentrations found in real-water streams, usually bellow 5 ppm.

Further research is needed to fully understand the electronic properties and enhanced photocatalytic activity of the MTV-UiO-66 variants in comparison to the expected average response of single-functional materials. One of the possible hypothesis under research by our team is that proton, electron, and hole transfer within the MTV-UiO-66 is enhanced due to the concurrent presence of electron donating and withdrawing groups within the framework, as initially pointed out by the photoconduction experiments.

2.6. Stabilization of chromium in MTV-MOFs

Chromium speciation after adsorption and photo-catalysis was studied by means of UV-Vis and EPR spectroscopies. In order to enhance the chromium UV-Vis and EPR signals, the experiments were performed with 100 ppm Cr^{VI} solutions.

First, the color change of the samples was noted both after the adsorption step in darkness and after UV illumination (Figure S34). After adsorption, UiO-66-NO_2 and UiO-66-NH_2-NO_2 materials get the characteristic yellow color of chromate anions. For the variants including amine and hydroxyl functionalities, the color change after Cr^{VI} adsorption is even more dramatic, especially for multivariate UiO-66-NH_2-$(OH)_2$ and UiO-66-NH_2-$(OH)_2$-NO_2,

becoming light brown. This darkening in the color of the samples is more severe under exposure to more to UV-radiation, which is indicative of electron transfer between Cr^{VI} and Cr^{III} mixed-valence species stabilized within the frameworks. In parallel, the color of the Cr^{VI} solutions was monitored as well. It is interesting to point that there is an appreciable decrease in intensity of the yellow color of the solution for almost all samples after photocatalysis, i.e. the intensity of the color of the Cr^{VI} solutions can be related with the efficiency of the materials to adsorb Cr^{VI} and catalyze the Cr^{VI} to Cr^{III} reduction. In line with previous results, the solutions after the photocatalysis with UiO-66 materials functionalized with hydroxyl groups display orange to brown dark hues, far from the yellow expected for Cr^{VI} solutions. Indeed, this deviation from the expected orange colour associated to chromate anions is explained by the dihydroxyterephthalate and Cr^{III} released to the solutions during photocatalysis experiments, in alignment with the previous results observed during the chemical stability assessments of UiO-66 and MTV-UiO-66 materials by UV-Vis (section 2.2). In order to confirm this point, the multivariate samples were digested and studied by ^{1}H-NMR after their use as photocatalysts. The integration of the ^{1}H-NMR signature of hydroxyl, nitro and amino-linkers indicates that there is a preferential leaching of hydroxyl-linkers in comparison to amino and nitro ones; the molar percentage of the linkers in the MTV-MOFs changes considerably after their working period, as described observed in the table 2. This experiment confirms the preference of hydroxyl-linkers to be solubilized at acidic conditions, but does not give clues about the release of BDC-NO_2 struts, in contrast with the observations obtained by UV-Vis spectroscopy. Although further research is needed to fully understand this counterintuitive difference, it is important to note that the release of zirconium ions from the UiO-66 framework could give rise to an additional absorbance of the UV-Vis signal in the same wavelength range (i.e. < 250 nm) that is used in this work to estimate the BDC-NO_2 concentration.[72] This would lead to an overestimation of the release calculated for BDC-NO_2 linkers, but does not refuse the fact that even when the stability of UiO-66-NO_2 is studied by UV-Vis spectroscopy, a non-negligible signal is observed at 250 nm, which confirms the partial release of nitro linkers jointly with zirconium ions into the aqueous solutions. In addition, the presence of chromium ions, and the illumination during photocatalysis, can alter as well the selective release of the linkers studied under ideal conditions in the previous sections.

Table 2. Molar percentage of amino, hydroxy and nitro linkers before and after their use as photocatalysts.

	BDC-NH_2 (%)	BDC-$(OH)_2$ (%)	BDC-NO_2 (%)
	(initial % / after operation)		

UiO-66-NH_2-$(OH)_2$	56 / 63	44 / 37	---
UiO-66-NH_2-NO_2	46 /45	---	54 / 55
UiO-66-$(OH)_2$-NO_2	---	41/ 35	59 / 65
UiO-66-NH_2-$(OH)_2$-NO_2	34 / 39	26 / 16	40 / 45

UV-Vis spectra of powdered UiO-66-R materials after Cr^{VI} adsorption and Cr^{VI} to Cr^{III} photo-reduction show the common fingerprint bands (~ 37000 cm^{-1}) attributed to the ligand-to-metal charge transfer (LMCT) (Figure 6a and Figure S35). An additional band, located around 26500 cm^{-1}, is observed for the materials containing amino or hydroxy functionalities. This signal is associated with the electron density transfer from the hydroxy and amine groups to the π* orbitals of the benzene ring; which gives the characteristic yellow color to UiO-66-NH_2 and UiO-66-$(OH)_2$. After Cr^{VI} adsorption, the UV-Vis spectra show additional adsorption bands related to Cr^{VI} and Cr^{III} species. Cr^{6+}-O^{2-} charge transfer bands for mono-chromate species are found at 35000 and 27000 cm^{-1}, and in our case, they overlap significantly with the UV-Vis signals coming from the MOF materials. The absorption band located around 17000 cm^{-1} confirms the presence of Cr^{III} species even after the adsorption stage. Thus, the amine, and especially the hydroxyl functionalities incorporated within the UiO-66 frameworks, trigger the Cr^{VI} to Cr^{III} chemical reduction in dark conditions. The intensity ascribed to the Cr^{III} UV-Vis signature increases in almost all samples after photocatalysis, but especially in UiO-66-NH_2, UiO-66-NH_2-$(OH)_2$ and UiO-66-NH_2-$(OH)_2$-NO_2. This evidence further confirms that during the Cr^{VI} to Cr^{III} photo-transformation, most of the Cr^{III} ions are stabilized within the porous frameworks (Figure 6a and Figure S35).

The results obtained from EPR spectroscopy support the conclusions drawn by UV-Vis spectroscopy (Figure 6b-i). For instance, EPR can be used as a complementary tool to study the transient Cr^{V} and final Cr^{III} species once inmobilized within the porous structures of the MOFs. Jointly with the information obtained from UV-Vis, EPR gives access to obtain a precise description of the chromium immobilization and transformation during adsorption and photocatalysis. Regarding EPR, three different signals associated with Cr^{III} and Cr^{V} species are observed after adsorption and photoreduction experiments, as illustrates schematically in the Figure 6b and 6c[73–75]:

1) The **y-signal** is an axially symmetric intense and sharp absorption band located around 3400 G. It is usually ascribed to isolated Cr^{V} intermediate and highly reactive species, which usually exhibit a highly distorted octahedral or pseudo-pyramidal coordination environment. The y-signal shows a characteristically sharp $g_{\perp}$=1.979 (~ 3390 G) and a weak somewhat diffuse g_{II} 1.961 (~ 3425 G) lines. (Figure 6c).

2) The **ϱ-signal** is a dispersed absorption band (~ 1350, $g_{\perp}$ ~ 5) associated with Cr^{III} ions immobilized as isolated species (Figure 6b). From an EPR perspective, isolated Cr^{III} ions are the ones that are far enough from surrounding Cr^{III} to establish strong enough ferro or antiferromagnetic interactions.
3) The **ß-signal** is a broad isotropic band related to clustered Cr^{III} ions, whose g value strongly depends on the size and shape of the chromium clusters. The presence of this characteristic EPR fingerprint indicates that the Cr^{III} ions are immobilized within the UiO-66 matrix close enough to establish magnetic interactions (i.e. Cr^{III}-O-Cr^{III} or Cr^{III}-OH···O-Cr^{III}, (Figure 6b).

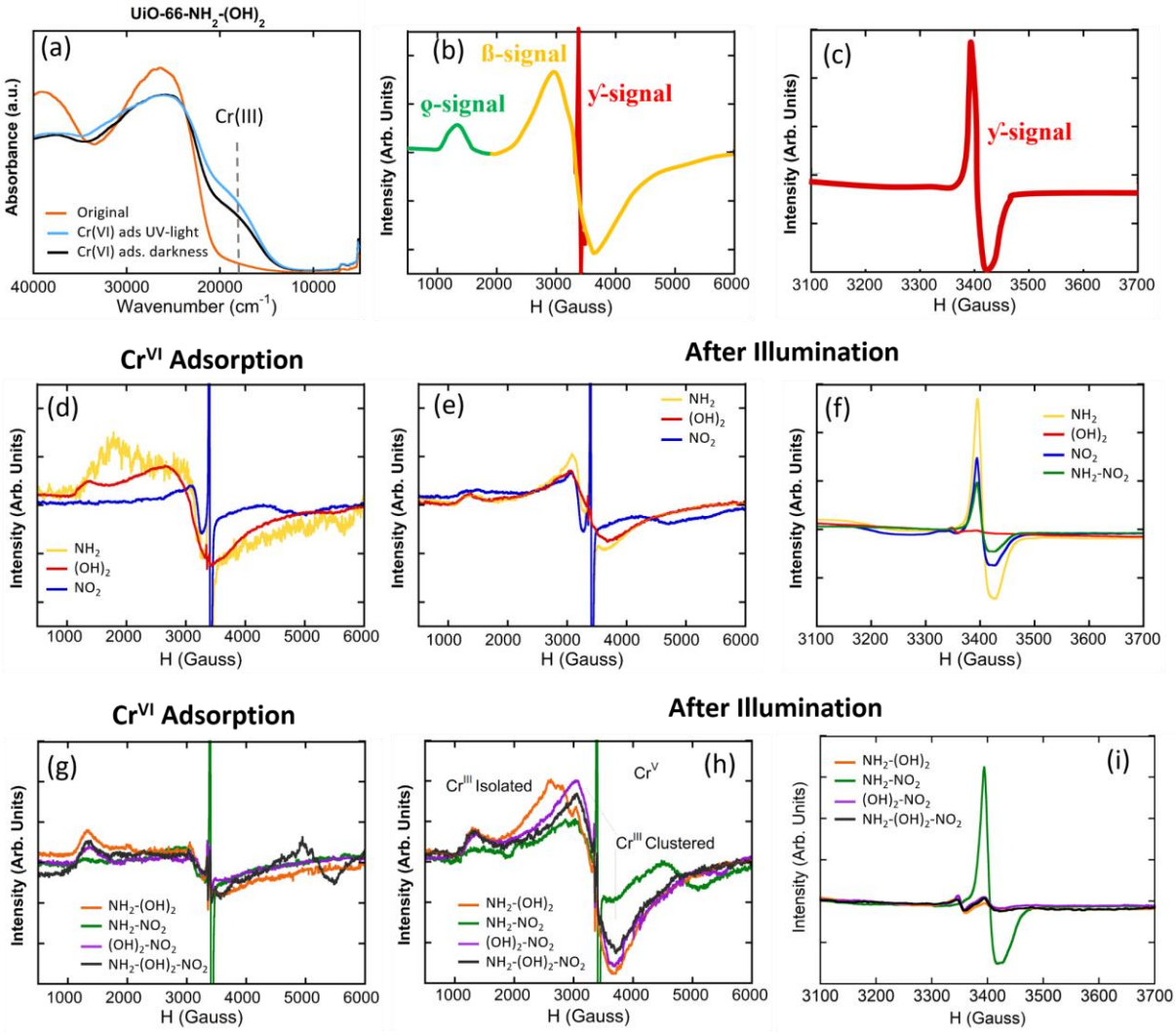

Figure 6. (a) UV-Vis spectra of UiO-66-NH_2-$(OH)_2$ pristine material and after the Cr^{VI} adsorption and Cr^{VI} to Cr^{III} photo-reduction. (b-c) Illustration of the ϱ, ß and y'-signals of the EPR spectra associated to Cr^{III} isolated and clustered ions, and intermediate Cr^{V} species, respectively (d-e) Detailed EPR spectra showing the ϱ-and ß-signals associated to Cr^{III} ions for single functionalized UiO-66-NH_2, -NO_2, -$(OH)_2$ frameworks after (d) Cr^{VI} adsorption and (e)

Cr^{VI} to Cr^{III} photoreduction. (f) Detailed EPR spectra showing the y-signal associated to Cr^{V} of single-functionalized UiO-66 materials after illumination. (g-h) Detailed EPR spectra showing the ϱ-and ß-signals associated to Cr^{III} ions for MTV-UiO-66 materials after (g) Cr^{VI} adsorption and (h) Cr^{VI} to Cr^{III} photoreduction. (i) Detailed EPR spectra showing the y-signal associated to Cr^{V} of MTV-UiO-66 materials after illumination.

After Cr^{VI} adsorption, the EPR spectrum of single functionalized UiO-66-$(OH)_2$ shows the most intense ϱ-and ß-signals associated with the inmobilization of Cr^{III} isolated and clustered species, followed by the EPR-spectra of UiO-66-NH_2 and UiO-66-NO_2 (Figure 6d). This evidence further points to the capacity of hydroxyl, and in less extent amine groups installed within UiO-66 framework, to induce a chemical reduction of Cr^{VI} to Cr^{III} during adsorption. Multivariate MOFs including hydroxyl functionalities also exhibit Cr^{VI} to Cr^{III} chemical reduction capacity, as derived from their EPR spectra. After adsorption, Cr^{III} ions are mainly stabilized as isolated ions within the porous framework (ϱ-signal – Figure 6g). Once illuminated, the intensity of the ß-signal associated with Cr^{III} clustered species increases for all the studied materials, but especially for MTV-UiO-66 exhibiting good Cr^{VI} to Cr^{III} photoreduction activity (Figure 6e and 6h). Overall, the presence of the EPR signals associated to Cr^{III} ions confirm that they are immobilized within the MOF's pore structure after photocatalysis, preventing their migration to the water media during the experiments.

Regarding the y-signal associated to Cr^{V} transient species, this is mainly found in the EPR spectra at -NO_2 and -NH_2 single variants of UiO-66 (Figure 6f), as well as at bi-functional UiO-66-NH_2-NO_2 multivariate MOF. Although UV illumination slightly reduces the intensity of the y-signal associated with Cr^{V}, it is still clearly visible after photo-catalysis (Figure 6i). In comparison, any incorporation of hydroxyl groups within the frameworks, even in the case of the trifunctional UiO-66-NH_2-$(OH)_2$-NO_2 material, gives rise to the disappearance of the y-signature associated to Cr^{V} (Figure 6f and 6i). We hypothesize that the presence of electron donor functionalities (i.e. hydroxyl or amino) destabilize the intermediate and highly reactive pentavalent chromium, quickly reducing it to Cr^{III} (Figure 6b). This is a crucial observation when MOF materials are applied for water remediation purposes since pentavalent ions are even more reactive and hazardous than Cr^{VI}. It is important to highlight that Cr^{VI} is silent by EPR, so despite that the presence of Cr^{III} and Cr^{V} has been duly confirmed by this technique, the evidence does not preclude the fact that hexavalent chromium is concurrently stabilized with Cr^{VI} and Cr^{III} ions within the MOFs after operation, as detailed by UV-Vis analyses.

2.7. Mechanisms for the chemical and photocatalytic transformation and immobilization of Cr^{VI} to Cr^{III}

The description of the overall transformation of Cr^{VI} species immobilized within a porous matrixes needs to consider that the modification of the chromium oxidation state is linked to variation in its coordination environment (Figure 7a). Overall, Cr^{VI} stabilized as CrO_4^{2-} chromate anions gains three electrons and incorporates two hydroxyl or water molecules within its coordination environment during its reduction to Cr^{III}. During this process, the highly reactive and transient intermediate Cr^{V} species are formed as well, as proved by EPR. As Cr^{V} is usually stabilized as a penta or hexa/coordinated species, during the chromate reduction to Cr^{V}, at least a water molecule need to be incorporated within the coordination sphere of the chromium ions (Figure 7a).

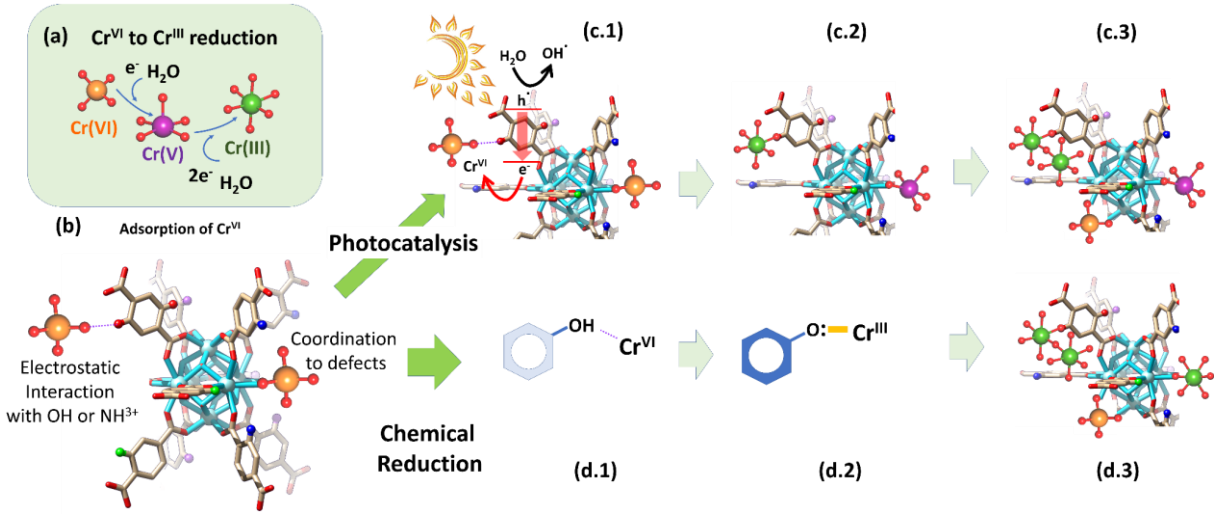

Figure 7. Cr^{VI} to Cr^{III} chemical and photoreduction mechanisms in MTV-UiO-66 dual sorbent/photocatalysts. (a) Overall Cr^{VI} to Cr^{III} reduction including Cr^{V} intermediate species. (b) Adsorption mechanisms for Cr^{VI} oxyanions within the MTV-UiO-66 frameworks. (c.1) light triggered generation of electron and holes and the concurrent electron transfer from the UiO-66-R framework to Cr^{VI} oxyanions. (c.2-c.3) Evolution of the chromium species into the porous frameworks during photocatalysis. (d.1) Electrostatic interaction between hydroxyl groups and Cr^{VI} ions. (d.2) Chemical reduction of Cr^{VI} to Cr^{III} and their stabilization into electron rich quinone groups. (d.3) Chromium speciation within the UiO-66 framework after the chemical reduction of Cr^{VI} to Cr^{III}, and their coordination to electron rich quinone groups derived from hydroxyl functions. (d.4) Possible chromium speciation without Cr^{V} transient species within UiO-66 frameworks containing hydroxyl groups.

The first step of the immobilization and transformation of Cr^{VI} to Cr^{III} into the UiO-66 frameworks is the adsorption of chromate anions (Figure 7b). Two possible mechanisms explain chromate adsorption capacity of the UiO-66 frameworks, their covalent inmobilization to the linker defective positions located at the zirconium hexanuclear clusters, or their electrostatic interaction with hydroxyl, but especially, with amine protonated groups. Reached at this point, two possible paths for the Cr^{VI} to Cr^{III} reduction are possible: *i*) photocatalysis and *ii*) chemical reduction.[76] The chemical encoding of the UiO-66 frameworks determine the efficiency and combination of the separated paths.

During photocatalysis, the light harvesting capacity of the UiO-66 frameworks (i.e. band gap) promotes the electron and holes separation, but their posterior conduction and transfer to the chromium ions is governed by the photoconduction efficiency of the materials (Figure 7c.1). At this point, the chemical variance of MTV materials makes the difference, because the incorporation of electro donor and withdrawing groups within the same framework improves the photoconduction and fasten the Cr^{VI} to Cr^{III} phototransformation. The chromate anions stabilized within the porous scaffold are steadily reduced to Cr^{V} and Cr^{III} while are immobilized into their adsorption position (Figure 7c.2). As the photocatalytic transformation of Cr^{VI} to Cr^{III} evolves, the Cr^{VI} to Cr^{III} photoreduction process is repeated leading to the clustering of Cr^{III} ions within the framework (Figure 7c.3). It is important to note at this point that if the single or MTV-UiO-66 lacks hydroxyl groups, transient Cr^{V} species will be stabilized within the material after operation. In contrast, when hydroxyl functionalities are encoded in UiO-66, the Cr^{VI} adsorption process (Figure 7b and d.1) is coupled to its chemical reduction to Cr^{III} via electron rich quinone groups coming from hydroxyl functionalities (Figure 7d.2). For instance, in addition to the EPR signatures associated to chromium, we have found as well the presence of a small EPR signal that could be associated to an organic quinone radical in the hydroxylated materials, but further analysis is needed to fully confirm this evidence. Finally, as the chemical reduction, or its combination with photocatalysis, evolves, chromium ions are stabilized as clusteres Cr^{III} ions with the frameworks (Figure 7d.3). Regardless if photocatalysis, chemical reduction or their combination is the process that triggers the Cr^{VI} transformation to Cr^{III}, the presence of hydroxyl ions is key to destabilize Cr^{V} transient species and transform them into Cr^{III} ions. This does not preclude the presence of Cr^{VI} and Cr^{III} ions within this hydroxyl-functionalized frameworks, but the absence of highly reactive and toxic Cr^{V}.

3. Conclusion

In this work, multivariate functionalization of Zr-UiO-66 framework with -NH_2, -$(OH)_2$ and -NO_2 functional groups has been used to create a new MOF material with enhanced Cr^{VI} and Cr^{III} adsorption capacity and excellent Cr^{VI} to Cr^{III} photoreduction efficiency. The integral functionalization of UiO-66 frameworks has given rise to a synergistic enhancement of the band gap, photoconduction and photocatalytic efficiency of the multivariate frameworks, which exceed properties of the the single functionalized materials. Trifunctional UiO-66-NH_2-$(OH)_2$-NO_2 exhibits; *i*) 99% Cr^{VI} to Cr^{III} photo-reduction in two hours, *ii*) photocatalysis and adsorption kinetics nearly as good as the UiO-66-$(OH)_2$ framework, *iii*) great capacity to retain the photo transformed Cr^{III} ions within the framework, *iv*) only negligible amounts of the highly reactive and hazardous Cr^{V} intermediate species after operation. MTV-reticular chemistry has been revealed as a limited tool to control the thermal and hydrolytic stability of UiO-66 type frameworks. Nevertheless, our findings can open the avenue to control the selective leaching of the linkers from multivariate UiO-66 frameworks to generate defects in these materials. Overall, multivariate reticular chemistry has shown to be an outstanding tool to tune the physico-chemical properties of UiO-66 frameworks in environmental applications, a strategy that can be easily adapted to other research fields such as controlled adsorption/desorption of target molecules i.e. drugs, modulation of optoelectronic properties, or controllable MOF degradation profiles under specific surrounding biological conditions, or multivariate catalytic pockets approaching the ones of enzymes.

4. Experimental Section

Synthesis of materials: UiO-66 MOFs were prepared through a slightly modified solvothermal synthesis based on the previously reported one by Audu *et. al*[56]. First, zirconium (IV) chloride (2.3 mmol, 0.5418 g) was dissolved in 30 mL N, N-Dimethylformamide (DMF) under magnetic stirring in a Pyrex® autoclave. Subsequently 2.3 mmol of the terephthalic, 2-aminoterepthalic, 2-nitroterepthalic or 2,5-dihydroxyterepthalic ligands were dissolved in 30 mL of DMF. In the specific case of multivariate (MTV) samples, a mixture of the different ligands where dissolved in 30 mL of DMF. For bifunctional MTV materials, 1.15 mmol of each linker was added to the DMF solution; while for trifunctional UiO-66-NH_2-$(OH)_2$-NO_2, 0.767 mmols of each linker were dissolved in 30 mL of DMF. Afterwards, 1.5 mL of distilled water was added as a modulator to the mixture. The Pyrex® reactor was closed and placed in a preheated oven at 80 °C for 24 h. The obtained solid was recovered by centrifugation (6000 rpm, 30 min) and afterwards washed three times for three consecutive days with methanol. Finally, the samples where dried at 120 °C during 24 h.

Materials' general characterization protocols: UiO-66-R variants were characterized by X-ray diffraction, infrared spectroscopy, UV-Vis spectroscopy, thermogravimetry and N_2 sorption at 77 K. A detailed description of the sample preparation, data curation and analysis can be found in the supplementary material. The percentage of each ligand was calculated thanks to ^{1}H-NMR spectroscopy of the digested samples.

Photo- and Electrochemical measurements: Photoconductivity and Mott-Schottky measurements were measured using a Biologic impedance analyser, in a standard three-electrode configuration with the sample as the working electrode, Ag/AgCl in 3 M KCl as reference electrode, a Pt sheet as the counter electrode, and a 0.2 M Na_2SO_4 aqueous solution, with a pH of 7, as the electrolyte. The samples consist of thin films of the UiO-66-R variants deposited on a transparent and conductive F:SnO_2 (FTO) coated glass. The samples were prepared by spin coating. First, the FTO coated glass was sequentially cleaned by 10 minutes of ultrasonication in hellmanex solution, acetone, isopropanol and distil water separately. The UiO-66-R variants were dispersed in methanol with a 10 mg/ml concentration. 50 µL of each dispersion was spun coated on a different FTO coated glass at 1000 rpm for 30 s, delimiting an active area of 1.5 cm^2. For the Photoconductivity measurements, the system was maintained under short-circuit (0 V vs Ag/AgCl), and the samples were submitted to illumination – dark cycles of 30 s, using a 150 W halogen lamp. Mott-Schottky measurements were taken under dark, using a 20 mV AC perturbation at 1000 Hz in a range of voltage from -1 to 1 V vs Ag/AgCl. The range of voltage where the recombination in the depletion region dominates is used to fit the flat band potential.

Chemical stability of the materials: To assess the chemical stability of the materials, 30 mg of the samples were immersed in water solutions (15 mL) with different acidities (pH 4, 7, 9 and 12). After that, they were cleaned with methanol and dried at 80 °C. Then, the solids were analysed by X-ray diffraction. The remnant solutions after the stability experiments were studied by liquid UV-Vis. The absorbance at 250 nm and 350 nm were taken as a reference to monitor the concentration of the organic linkers leached to the aqueous media. The quantification of the organic linker concentration in the media was determined via the calibration curves of the individual organic linkers (Figure S31-S33). The % of the linker released was determined following the protocol described in the supporting information – section S3.2.

Adsorption kinetics of Cr^{VI} and Cr^{III} ions: To study the adsorption kinetics of our materials towards Cr^{VI} and Cr^{III}, 6 mg of UiO-66-R samples were immersed in 24 mL of Cr^{VI} or Cr^{III}

solutions with a 5 ppm concentration. The samples were then filtered with a 0.22 µm-pored filter and measured by ICP-AES.

Bifunctional Photocatalytic reduction of Cr^{VI} to Cr^{III} coupled to Cr(III) adsorption: A 365 nm lamp was used to trigger the photocatalytic activity of UiO-66-R variants studied in this work. 35 mg of the samples were placed in 140 mL of Cr^{VI} solutions. The initial Cr^{VI} concentration was tuned between 14 and 12 ppms in order to obtain a similar Cr^{VI} concentration at the initial point of the photocatalysis experiments, and after the adsorption in dark conditions for 2 hours. After illumination, 0.5 mL aliquots were taken at different times of the reaction (5, 10, 15, 30, 45, 60, 120 and 240 min), filtered with a 0.22 µm pore filter. The Cr^{VI} concentration was measured by 1,5-Diphenylcarbazide colorimetric method. The overall chromium concentration of the solutions was determined by ICP-AES. Cr^{III} content of the aliquotes was determined by the subtraction between the total chromium concentration obtained by ICP-AES and the Cr^{VI} concentration determined by 1,5-Diphenylcarbazide protocol.

EPR study of the chromium speciation stabilized within the UiO-66-R variants: Electronic paramagnetic resonance (EPR) spectra were recorded at room temperature using a Bruker ELEXSYS 500 spectrometer (X band). The samples were placed in quartz tubes. In order to stablish a qualitative comparison, approximately the same amount of sample and packing degree within the quartz tubes was used in all cases. The magnetic field was calibrated by a S4 nuclear magnetic resonance (NMR) probe and the frequency inside the cavity (~9.395 GHz) was determined with an integrated micro wave frequency.

Supporting Information

Supporting Information is available from the Wiley Online Library or from the author.

Acknowledgements

The authors thank financial support from the Spanish Ministry of Economy and Competitiveness (MINECO) through the projects MAT2016-76039-C4-3-R and PID2020-115935RB-C42 (AEI/FEDER, UE) (including FEDER financial support) and from the Basque Government Industry and Education Departments under the ELKARTEK, HAZITEK and PIBA (PIBA-2018-06) programs, respectively. Ainara Valverde acknowledges the Basque Government (Education Department) for her PhD grant (PREB_2018_1_004). David Payno Zarceño acknowledges the Spanish Ministry of Science and Innovation (PARASOL, RTI2018-102292-B-100) for his pre-doctoral contract. The European Union´s Horizon 2020 research & Innovation programmes is also acknowledged for the funding of the H2020-MSCA-RISE-2017

INDESMOF (Ref.: 778412) and LC-SC3-RES-25-2020 4AirCRAFT (Ref. :101022633) projects. In addition, 4AirCRAFT project is also supported by Japan Science and Technology Agency (JST) and Mission Innovation Challenge supported by the Sao Paulo Research Foundation (FAPESP). The authors thank the technical and human support provided by SGIker (UPV/EHU).

Received: ((will be filled in by the editorial staff))
Revised: ((will be filled in by the editorial staff))
Published online: ((will be filled in by the editorial staff))

References

[1] M. A. Barakat, *Arab. J. Chem.* **2011**, *4*, 361.

[2] W. Zhang, D. Zhang, Y. Liang, *Environ. Pollut.* **2019**, *247*, 266.

[3] P. B. Tchounwou, C. G. Yedjou, A. K. Patlolla, D. J. Sutton, in *Mol. Clin. Envirnmental Toxicol.*, **2012**, pp. 133–164.

[4] F. Ke, L. G. Qiu, Y. P. Yuan, F. M. Peng, X. Jiang, A. J. Xie, Y. H. Shen, J. F. Zhu, *J. Hazard. Mater.* **2011**, *196*, 36.

[5] N. Yin, K. Wang, L. Wang, Z. Li, *Chem. Eng. J.* **2016**, *306*, 619.

[6] Y. Wang, G. Ye, H. Chen, X. Hu, Z. Niu, S. Ma, *J. Mater. Chem. A* **2015**, *3*, 15292.

[7] M. Mon, X. Qu, J. Ferrando-Soria, I. Pellicer-Carreño, A. Sepulveda-Escribano, E. V. Ramos Fernandez, J. C. Jansen, D. Armentano, E. Pardo, *J. Mater. Chem. A* **2017**, *5*, 20120.

[8] M. Mon, F. Lloret, J. Ferrando-Soria, C. Marta--Gastaldo, D. Armentano, E. Pardo, *Angew. Chemie - Int. Ed.* **2016**, *55*, 11167.

[9] H. Zhao, Q. Xia, H. Xing, D. Chen, H. Wang, *ACS Sustain. Chem. Eng.* **2017**, *5*, 4449.

[10] J. Hu, G. Chen, I. M. C. Lo, *Water Res.* **2005**, *39*, 4528.

[11] P. G. Saiz, N. Iglesias, B. González Navarrete, M. Rosales, Y. M. Quintero, A. Reizabal, J. Orive, A. Fidalgo Marijuan, E. S. Larrea, A. C. Lopes, L. Lezama, A. García, S. Lanceros-Mendez, M. I. Arriortua, R. Fernández de Luis, *Chem. - A Eur. J.* **2020**, *26*, 13861.

[12] A. Maleki, B. Hayati, M. Naghizadeh, S. W. Joo, *J. Ind. Eng. Chem.* **2015**, *28*, 211.

[13] S. Rengaraj, S. Venkataraj, J. W. Yeon, Y. Kim, X. Z. Li, G. K. H. Pang, *Appl. Catal. B Environ.* **2007**, *77*, 157.

[14] C. C. Wang, X. D. Du, J. Li, X. X. Guo, P. Wang, J. Zhang, *Appl. Catal. B Environ.*

2016, *193*, 198.

[15] Y. Wang, N. Zhang, D. Chen, D. Ma, G. Liu, X. Zou, Y. Chen, R. Shu, Q. Song, W. Lv, *Sci. Total Environ.* **2019**, *682*, 118.

[16] G. K. Kinuthia, V. Ngure, D. Beti, R. Lugalia, A. Wangila, L. Kamau, *Sci. Rep.* **2020**, *10*, 1.

[17] P. G. Saiz, A. Valverde, B. Gonzalez-Navarrete, M. Rosales, Y. M. Quintero, A. Fidalgo-Marijuan, J. Orive, A. Reizabal, E. S. Larrea, M. I. Arriortua, S. Lanceros-Méndez, A. García, R. Fernández de Luis, *Catalysts* **2021**, *11*, 51.

[18] R. G. Saiz, P., Iglesias, N., Gonzalez-Navarrete, B., Rosales, M., Quintero, Y. M., Reizabal, A., Orive, J., Fidalgo-Marijuan, A., Lanceros-Mendez, S., Arriortua, M. I.,& Fernandez de Luis, *Chem. Eur. J.* **2020**, *26*, 1.

[19] X. D. Du, X. H. Yi, P. Wang, W. Zheng, J. Deng, C. C. Wang, *Chem. Eng. J.* **2019**, *356*, 393.

[20] Y. Zhang, M. Xu, H. Li, H. Ge, Z. Bian, *Appl. Catal. B Environ.* **2018**, *226*, 213.

[21] Y. H. Li, X. H. Yi, Y. X. Li, C. C. Wang, P. Wang, C. Zhao, W. Zheng, *Environ. Res.* **2021**, *201*, 111596.

[22] C. E. Barrera-Díaz, V. Lugo-Lugo, B. Bilyeu, *J. Hazard. Mater.* **2012**, *223–224*, 1.

[23] A. Valverde, P. G.-Sainz, J. Orive, L. E., A. Reizabal-Para, G. Tovar, G. Copello, J. M. Lazaro-Martinez, B. Rodriguez, B. Gonzalez-Navarrete, M. Y. Quintero, M. Rosales, A. García, M. I. Arriortua, R. Fernandez de Luis, in *Adv. Light. Multifunct. Mater.*, Elsevier, **2020**, pp. 43–130.

[24] S. Massari, M. Ruberti, *Resour. Policy* **2013**, *38*, 36.

[25] M. Rosales, T. Zoltan, C. Yadarola, E. Mosquera, F. Gracia, A. García, *J. Mol. Liq.* **2019**, *281*, 59.

[26] J. Matos, M. Rosales, A. García, C. Nieto-Delgado, J. R. Rangel-Mendez, *Green Chem.* **2011**, *13*, 3431.

[27] M. Rosales, J. Orive, R. Espinoza-González, R. Fernández de Luis, R. Gauvin, N. Brodusch, B. Rodríguez, F. Gracia, A. García, *Chem. Eng. J.* **2021**, *415*, 128906.

[28] J. Li, X. Wang, E. Power, G. Zhao, Z. Chai, C. Chen, A. Alsaedi, T. Hayat, X. Wang, *Chem. Soc. Rev.* **2018**, *47*, 2322.

[29] M. Mon, R. Bruno, J. Ferrando-Soria, D. Armentano, E. Pardo, *J. Mater. Chem. A* **2018**, *6*, 4912.

[30] R. Freund, S. Canossa, S. M. Cohen, W. Yan, H. Deng, V. Guillerm, M. Eddaoudi, D. G. Madden, D. Fairen-Jimenez, H. Lyu, L. K. Macreadie, Z. Ji, Y. Zhang, B. Wang, F.

Haase, C. Wöll, O. Zaremba, J. Andreo, S. Wuttke, C. S. Diercks, *Angew. Chemie Int. Ed.* **2021**, *60*, 23946.

[31] H. Furukawa, K. E. Cordova, M. O'Keeffe, O. M. Yaghi, *Science (80-.).* **2013**, *341*, 123044.

[32] S. Patial, P. Raizada, V. Hasija, P. Singh, V. K. Thakur, V.-H. Nguyen, *Mater. Today Energy* **2021**, *19*, 100589.

[33] J. Bitzer, W. Kleist, *Chem. – A Eur. J.* **2019**, *25*, 1866.

[34] C. Gropp, S. Canossa, S. Wuttke, F. Gándara, Q. Li, L. Gagliardi, O. M. Yaghi, *ACS Cent. Sci.* **2020**, *6*, 1255.

[35] R. Freund, O. Zaremba, G. Arnauts, R. Ameloot, G. Skorupskii, M. Dincă, A. Bavykina, J. Gascon, A. Ejsmont, J. Gościańska, M. Kalmutzki, U. Lächelt, E. Ploetz, C. Diercks, S. Wuttke, *Angew. Chemie Int. Ed.* **2021**, *60*, 23975.

[36] J. Wu, J. Zhou, S. Zhang, A. Alsaedi, T. Hayat, J. Li, Y. Song, *J. Colloid Interface Sci.* **2019**, *555*, 403.

[37] J. H. Cavka, S. Jakobsen, U. Olsbye, N. Guillou, C. Lamberti, S. Bordiga, K. P. Lillerud, *J. Am. Chem. Soc.* **2008**, *130*, 13850.

[38] Q. Chen, Y. Feng, R. Tian, J. Chen, A. Wang, J. Yao, *Ind. Eng. Chem. Res.* **2019**, *58*, 21562.

[39] A. Dhakshinamoorthy, A. M. Asiri, H. García, *Angew. Chemie - Int. Ed.* **2016**, *55*, 5414.

[40] J. Bedia, V. Muelas-ramos, M. Peñas-garzón, A. Gómez-avilés, J. J. Rodríguez, C. Belver, *Catal* **2019**, *9*, 52.

[41] M. Kandiah, M. H. Nilsen, S. Usseglio, S. Jakobsen, U. Olsbye, M. Tilset, C. Larabi, E. A. Quadrelli, F. Bonino, K. P. Lillerud, *Chem. Mater.* **2010**, *22*, 6632.

[42] H. Deng, C. J. Doonan, H. Furukawa, R. B. Ferreira, J. Towne, C. B. Knobler, B. Wang, O. M. Yaghi, *Science (80-.).* **2010**, *327*, 846.

[43] T. M. Osborn Popp, O. M. Yaghi, *Acc. Chem. Res.* **2017**, *50*, 532.

[44] Y.-M. Li, J. Yuan, H. Ren, C.-Y. Ji, Y. Tao, Y. Wu, L.-Y. Chou, Y.-B. Zhang, L. Cheng, *J. Am. Chem. Soc.* **2021**, *143*, 15378.

[45] W. Schrimpf, J. Jiang, Z. Ji, P. Hirschle, D. C. Lamb, O. M. Yaghi, S. Wuttke, *Nat. Commun.* **2018**, *9*, 1647.

[46] I. Abánades Lázaro, C. J. R. Wells, R. S. Forgan, *Angew. Chemie - Int. Ed.* **2020**, *59*, 5211.

[47] Z. Dong, Y. Sun, J. Chu, X. Zhang, H. Deng, *J. Am. Chem. Soc.* **2017**, *139*, 14209.

[48] T. Y. Luo, C. Liu, X. Y. Gan, P. F. Muldoon, N. A. Diemler, J. E. Millstone, N. L. Rosi, *J. Am. Chem. Soc.* **2019**, *141*, 2161.

[49] S. Yuan, W. Lu, Y.-P. Chen, Q. Zhang, T.-F. Liu, D. Feng, X. Wang, J. Qin, H.-C. Zhou, *J. Am. Chem. Soc.* **2015**, *137*, 3177.

[50] Z. Hu, A. Gami, Y. Wang, D. Zhao, *Adv. Sustain. Syst.* **2017**, *1*, 1700092.

[51] M. Mon, R. Bruno, E. Tiburcio, M. Viciano-Chumillas, L. H. G. Kalinke, J. Ferrando-Soria, D. Armentano, E. Pardo, *J. Am. Chem. Soc.* **2019**, *141*, 13601.

[52] W. Fan, S. Yuan, W. Wang, L. Feng, X. Liu, X. Zhang, X. Wang, Z. Kang, F. Dai, D. Yuan, D. Sun, H.-C. Zhou, *J. Am. Chem. Soc.* **2020**, *142*, 8728.

[53] H. Lyu, Z. Ji, S. Wuttke, O. M. Yaghi, *Chem* **2020**, *6*, 2219.

[54] H. Furukawa, U. Müller, O. M. Yaghi, *Angew. Chemie - Int. Ed.* **2015**, *54*, 3417.

[55] A. Ejsmont, J. Andreo, A. Lanza, A. Galarda, L. Macreadie, S. Wuttke, S. Canossa, E. Ploetz, J. Goscianska, *Coord. Chem. Rev.* **2021**, *430*, 213655.

[56] C. O. Audu, H. G. T. Nguyen, C. Y. Chang, M. J. Katz, L. Mao, O. K. Farha, J. T. Hupp, S. T. Nguyen, *Chem. Sci.* **2016**, *7*, 6492.

[57] Y. Gu, D. Xie, Y. Ma, W. Qin, H. Zhang, G. Wang, Y. Zhang, H. Zhao, *ACS Appl. Mater. Interfaces* **2017**, *9*, 32151.

[58] M. M. Modena, B. Rühle, T. P. Burg, S. Wuttke, *Adv. Mater.* **2019**, *31*, 1.

[59] P. Hirschle, T. Preiß, F. Auras, A. Pick, J. Völkner, D. Valdepérez, G. Witte, W. J. Parak, J. O. Rädler, S. Wuttke, *CrystEngComm* **2016**, *18*, 4359.

[60] N. C. Burtch, H. Jasuja, K. S. Walton, *Chem. Rev.* **2014**, *114*, 10575.

[61] S. S. Chen, C. Hu, C.-H. Liu, Y.-H. Chen, T. Ahamad, S. M. Alshehri, P.-H. Huang, K. C.-W. Wu, *J. Hazard. Mater.* **2020**, *397*, 122431.

[62] Y. Liu, S. Lin, Y. Liu, A. K. Sarkar, J. K. Bediako, H. Y. Kim, Y. Yun, **2019**, *1805242*, 1.

[63] P. GSaiz, A. C. Lopes, S. Eizagirre Barker, R. Fernández de Luis, M. I. Arriortua, *Mater. Des.* **2018**, *155*, DOI 10.1016/j.matdes.2018.06.013.

[64] K. Leus, T. Bogaerts, J. De Decker, H. Depauw, K. Hendrickx, H. Vrielinck, V. Van Speybroeck, P. Van Der Voort, *Microporous Mesoporous Mater.* **2016**, *226*, 110.

[65] T. D. Bennett, A. K. Cheetham, *Acc. Chem. Res.* **2014**, *47*, 1555.

[66] A. J. Howarth, Y. Liu, P. Li, Z. Li, T. C. Wang, J. T. Hupp, O. K. Farha, *Nat. Rev. Mater.* **2016**, *1*, 1.

[67] X. Mu, J. Jiang, F. Chao, Y. Lou, J. Chen, *Dalt. Trans.* **2018**, *47*, 1895.

[68] L. Shen, S. Liang, W. Wu, R. Liang, L. Wu, *Dalt. Trans.* **2013**, *42*, 13649.

[69] S. Iqbal, Z. Pan, K. Zhou, *Nanoscale* **2017**, *9*, 6638.

[70] Q. Liang, S. Cui, C. Liu, S. Xu, C. Yao, Z. Li, *J. Colloid Interface Sci.* **2018**, *524*, 379.

[71] S. Rapti, A. Pournara, D. Sarma, I. T. Papadas, G. S. Armatas, Y. S. Hassan, M. H. Alkordi, M. G. Kanatzidis, M. J. Manos, *Inorg. Chem. Front.* **2016**, *3*, 635.

[72] X. Sun, J. Ma, X. Chen, Z. Li, C. Deng, B. Liu, *J. Sol-Gel Sci. Technol.* **2018**, *86*, 431.

[73] V. Daier, S. Signorella, M. Rizzotto, M. I. Frascaroli, C. Palopoli, C. Brondino, J. M. Salas-Peregrin, L. F. Sala, *Can. J. Chem.* **1999**, *77*, 57.

[74] B. V. Padlyak, J. Kornatowski, G. Zadrozna, M. Rozwadowski, A. Gutsze, *J. Phys. Chem. A* **2000**, *104*, 11842.

[75] B. M. Weckhuysen, R. A. Schoonheydt, F. E. Mabbs, D. Collison, *J. Chem. Soc. - Faraday Trans.* **1996**, *92*, 2431.

[76] Z. Wang, J. Yang, Y. Li, Q. Zhuang, J. Gu, *Chem. - A Eur. J.* **2017**, *23*, 15415.

Table of contents

Multivariate functionalization of UiO-66 for photoreductive water remediation

A. Valverde, D. Payno, L. Lezama, J. M. Laza, S. Wuttke*, and R. Fernández de Luis*

A multivariate functionalization approach has been applied to UiO-66 framework in order to obtain a MOF material containing nitro, amino and hydroxyl functionalities. The balanced multivariate encoding allows a tailor-function design of a hydrolytic stable UiO-66 framework towards a fast Cr^{VI} to Cr^{III} photo-reduction and Cr^{III} immobilization.